Chapter 2
Recent Advances in Nanoplasmonics and Magnetoplasmonics

Maxim R. Shcherbakov, Tatyana V. Dolgova, and Andrey A. Fedyanin

Abstract Nanoplasmonics is a vastly developing area of modern photonics, which is capable of providing mankind with new routes to fast and miniature communication and technologies. With unprecedentedly high bandwidth supplied by photons and subwavelength dimensions supplied by electrons, surface plasmon is the next candidate for the everyday-life information unit. In this chapter we review recent advances in controlling the generation and propagation of surface plasmon polaritons in nanostructured materials as well as utilization of surface plasmons in order to obtain efficient control over optical signals.

2.1 Surface Electromagnetic Waves

Surface electromagnetic waves are defined as waves propagating along the interface between two media and existing in both of them [1, 2]. The dispersion law of the surface wave can be derived from Maxwell's equations by substituting the solution in the form of a localized wave (the *Oz* axis is perpendicular to the interface and directed towards the first medium, the *Ox* axis is at the interface, Fig. 2.1):

$$A = A_0 e^{s_{1,2} z} e^{i(\omega t - k_{spp} x)}, \tag{2.1}$$

where k_{spp} is the wave vector of the surface wave and $s_{1,\,2}$ are the extinction coefficients in the first and second media, respectively. If $\varepsilon_1(\omega)$ and $\varepsilon_2(\omega)$ are

M.R. Shcherbakov (✉) • T.V. Dolgova • A.A. Fedyanin
Faculty of Physics, Lomonosov Moscow State University, Moscow 119991, Russia
e-mail: shcherbakov@nanolab.phys.msu.ru; dolgova@nanolab.phys.msu.ru; fedyanin@nanolab.phys.msu.ru

A. Korkin and D.J. Lockwood (eds.), *Nanoscale Applications for Information and Energy Systems*, Nanostructure Science and Technology,
DOI 10.1007/978-1-4614-5016-0_2,

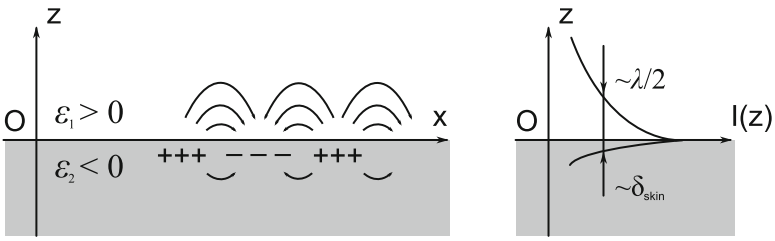

Fig. 2.1 *Left*: The interface between two media with the opposite signs of the real parts of the dielectric permittivity showing a schematic distribution of unbalanced charges and the electric field vector lines of the surface wave. *Right*: Intensity distribution and typical localization scales of the surface waves in the vicinity of the interface

complex dielectric constants of the first and second media, respectively, the dispersion relation takes the following form:

$$k_{spp}(\omega) = \frac{\omega}{c}\sqrt{\frac{\varepsilon_1(\omega)\varepsilon_2(\omega)}{\varepsilon_1(\omega)+\varepsilon_2(\omega)}}. \tag{2.2}$$

In the case of a metal surface in a dielectric environment, k_{spp} is an imaginary number and the surface wave is called surface plasmon polariton (SPP) since the unbalanced charges rise due to oscillations of free electrons of metal. In general k_{spp} can be written as:

$$k_{spp}(\omega) = k'(\omega) + ik''(\omega) = \frac{\omega}{c}\sqrt{\frac{\varepsilon_2'(\omega)\varepsilon_1}{\varepsilon_2'(\omega)+\varepsilon_1}} + \frac{i\omega}{c}\left(\frac{\varepsilon_2'(\omega)\varepsilon_1}{\varepsilon_2'(\omega)+\varepsilon_1}\right)^{3/2}\frac{\varepsilon_2''(\omega)}{2(\varepsilon_2'(\omega))^2}. \tag{2.3}$$

Figure 2.2 shows a typical dispersion law of SPPs at the metal–air interface ($\varepsilon_1 = 1$) in the form of the expression (2.2). Here the dielectric function of metal is approximated with the Drude model:

$$\varepsilon_2(\omega) = 1 - \frac{\omega_p^2}{\omega^2}. \tag{2.4}$$

It should be noted that this model describes well the optical response of metals in the infrared region. However, the model is not valid in the ultraviolet and visible spectral ranges due to the presence of pronounced resonances associated with the interband electron transitions. Besides, the ohmic losses in the metal are not taken into account.

The value of the imaginary part of the SPP wave vector indicates the energy losses due to its transfer from the oscillating electrons to the lattice. The mean free path of SPPs at a smooth metal surface is described by:

$$L = \frac{1}{2k_{spp}''}, \tag{2.5}$$

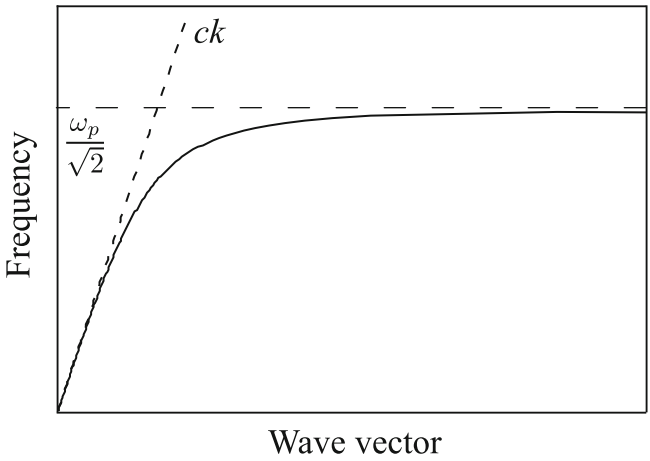

Fig. 2.2 The dispersion law of a surface plasmon polariton (*solid line*) and light in vacuum (*dotted line*)

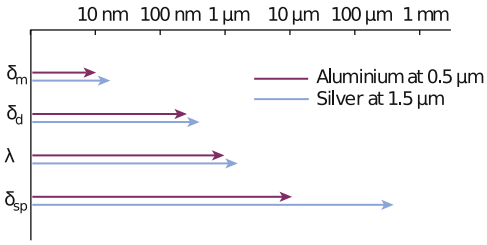

Fig. 2.3 Characteristic length scales of surface-plasmon-based photonics: the propagation length δ_{SP}, the decay length in the dielectric material δ_d, and the decay length in the metal δ_m [3]

where k_{spp} is the imaginary part of the SPP wave vector and is determined by the dielectric properties of the metal. For example, the free path of SPPs at the silver surface is approximately 1 mm for the telecommunication wavelength range ($\lambda \simeq 1.5$ µm). Figure 2.3 shows the comparison of typical scales of the SPP energy localization.

An important effect in nanoplasmonics is the resonant excitation of local plasmons (LPs). LP resonance can be observed in metallic particles with typical sizes much smaller than the optical wavelength for which the quasi-static approximation of the electromagnetic response is applicable. The polarizability $p(\omega)$ of a subwavelength particle is proportional to the local field factor [4, 5]:

$$p(\omega) \sim \frac{1}{L_i[\varepsilon_2(\omega) - \varepsilon_1] + \varepsilon_1}, \tag{2.6}$$

where $\varepsilon_2(\omega)$ is dielectric permittivity of the particle material, ε_1 is a dielectric constant of the environment, and L_i is a factor depending on the shape and size of

the particles and the polarization of the incident light ($i = x, y, z$). The denominator of Eq. (2.6) tends to zero at some wavelength leading to a resonance of local plasmon polaritons, i.e., to increase the average kinetic energy of electrons and to an increase in absorption due to scattering of electrons from the lattice of the metal. The coefficients L_i can be calculated as follows:

$$L_x = \int_0^\infty \frac{abc\ ds}{2(s+a)^{3/2}(s+b)^{1/2}(s+c)^{1/2}}, \tag{2.7}$$

where a, b, and c are the sizes of the particles in the directions x, y, and z. The equations for L_y and L_z are obtained by cyclic permutation of the variables a, b, and c. The equation $\Sigma L_i = 1$ is fulfilled. The formulae for coefficients L_i for metallic ellipsoid with small cross-section are as follows:

$$L_x = 0, \quad L_y = \frac{c}{b+c}, \quad L_z = \frac{b}{b+c}. \tag{2.8}$$

2.2 Experimental Methods of Excitation of Surface Plasmons

If $\varepsilon_2 < 0$, $\varepsilon_1 > 0$ and $|\varepsilon_2| > \varepsilon_1$, which corresponds, e.g., to the case of a metal in a vacuum environment in the visible, $\mathrm{Re}(k_{\mathrm{spp}}) > \omega/c$. Thus, SPPs cannot be excited by light incident from medium 1. A number of optical schemes can be used to compensate for the difference in wave numbers (see Fig. 2.4).

The schemes with dielectric prisms, such as the Kretschmann or Otto schemes, are commonly used for efficient excitation of plasmon-polaritons (Fig. 2.4a, b). The exciting beam is incident from a medium with a refractive index greater than the index of one surrounding the film. The grating excitation schemes are also widespread (Fig. 2.5). Consider a metal surface modulated with the period of d that is irradiated with light of wavelength λ at an angle of incidence θ. The scattered radiation has a set of diffraction orders. The values of the wave vector projection to the plane of the grating for these orders are $k_x = k_0 \sin\theta + jG = 2\pi\ sin\theta/\lambda + 2\pi j/d$,

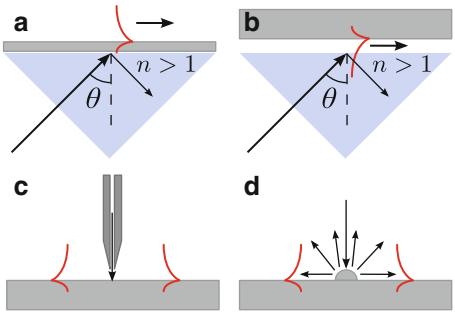

Fig. 2.4 Experimental methods for coupling light to surface plasmons. (**a**) Kretschmann geometry. (**b**) Otto geometry. (**c**) Coupling SPP with a scanning near-field optical microscope tip. (**d**) Surface nanodefect coupling

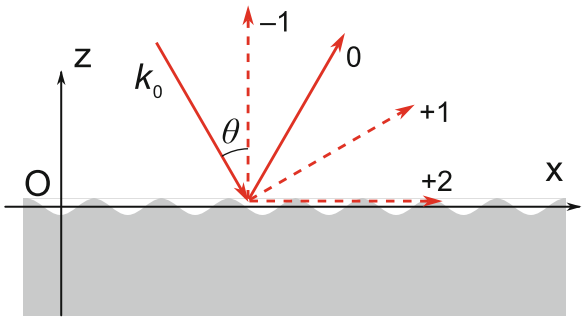

Fig. 2.5 Diffraction of electromagnetic radiation from a metallic diffraction grating and SPP coupling through +2 diffraction order

where G is the grating reciprocal vector, and j is an integer. If the wave number of any diffracted beam coincides with the wave number of SPP:

$$\pm k_{spp} = k_0 \sin\theta + jG, \tag{2.9}$$

the SPP is excited effectively. The central wavelength of the SPP coupled through the grating is written as follows:

$$\lambda = \frac{d}{\pm j}\left(\sqrt{\frac{\varepsilon_2'(\omega)\varepsilon_1}{\varepsilon_2'(\omega)+\varepsilon_1}} \mp \sin\theta\right). \tag{2.10}$$

The condition (2.10) leads to so-called Wood's anomaly [6] which manifests itself as a narrow dip in the reflectance spectra of the metal gratings [7]. Thus, the resonant excitation of surface plasmons in the optical wavelength range in metallic films is possible in the presence of periodic nanostructuring.

2.3 Experimental Methods of Detection of Surface Plasmons

Since SPP is an excitation with the wave vector greater than one in surrounding dielectric, it does not couple to propagating electromagnetic waves. In other words, one cannot use a conventional microscope to observe an SPP by taking an image of the metallic film surface. In order to identify the distribution of plasmonic waves as a function of the coordinate in the plane of the film, it is necessary to use one of methods that are described in this section, namely the leakage radiation microscopy or scanning near-field optical microscopy (SNOM).

The first method of SPP observation relies on the reciprocal character of the Kretschmann excitation scheme [8]. An SPP coupled to the surface of the film via a dielectric prism experiences losses—nonradiative ones and radiative ones. The former stands for ohmic losses due to electron-lattice energy exchange, while the latter emerges from SPPs coupling back to the far-field radiation, e.g., via the same

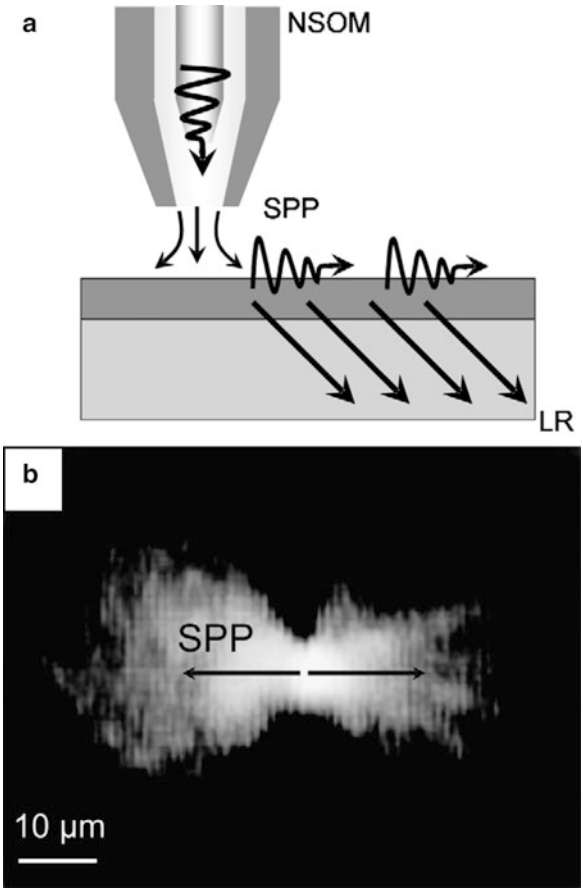

Fig. 2.6 Leakage radiation microscopy image of SPPs launched using a scanning near-field optical microscope tip [8]

channel it was excited. In other words, there would be radiation in the direction of the reflected ray in Fig. 2.4a which is present due to SPPs. Every point of the film subject to carrying SPP energy is giving part of the SPP energy back in proportion to the intensity of the SPP in that point. By taking an image of the film surface though the prism one can directly observe the SPP profile, as shown in Fig. 2.6.

Being one of the conventional far-field microscopy methods, leakage radiation microscopy has significant limitations associated with the diffraction of light. One of the fundamental laws of optics is the existence of the so-called diffraction limit, which determines the minimum distance R between two objects that are said to be resolved from each other using light of wavelength λ:

$$R \simeq 0.61\frac{\lambda}{n},$$

where n is the refraction index of the medium. The limit for the optical wavelength range is of the order of 200–300 nm. Scanning near-field optical microscopy is

based on other principles of the image construction, which can overcome the difficulties associated with diffraction of light and realize a spatial resolution of 10 nm and better.

The principles of SNOM lie in the use of a light detector with a size smaller than the wavelength of the radiation. The tip of an optical fiber covered with a thin metal layer with a small hole in it can form such a detector. The detector collects only the portion of the radiation in the vicinity of the hole; so the resolution of this method is determined by the size of the hole which can be made less than 100 nm [9]. The optical image is obtained by scanning the surface of the sample with the probe and constructing a two-dimensional raster of the optical signal value with a resolution exceeding the diffraction limit [10]. Since the distance between the probe and the sample surface is set to be small (starting from 5 nm) and kept constant during scanning, it is also possible to observe and measure the amplitude of the nonradiative excitations of the samples, such as SPP [11], or radiation reflected from the interface between two dielectrics under conditions of total internal reflection [12]. Many properties of plasmonic nanostructures and microsystems have been studied by means of SNOM, including nanofocusing [13], energy transfer along plasmon waveguides by means of SPPs [14, 15], interference of plasmon waves [16, 17], and others.

The same approach of bringing a point-like scatterer to the subwavelength vicinity of SPP is realized by adding subwavelength roughness to the metal surface. Every bump of the film acts like a SNOM tip scattering the SPP energy to the far-field. By taking an optical microscope image of the rough golden film, one can steadily observe the SPP intensity profile. The disadvantage of the method lies in the apparent distortion of the sample initial design as it is usually assumed to be made of a flat metallic film.

2.4 Plasmonic Metamaterials

The development of nanofabrication technology has led to a vast variety of new possibilities of tailoring of optical properties of media. Optical metamaterials are produced from bulk media or thin films by lithographic methods which imply spatial structuring on the scale of tens of nanometers. This gives rise to optical properties absent in the initial material. Negative refractive index [18] and many other noticeable effects were observed recently in optical metamaterials. Noble metals are a common basis for most of the optical metamaterials and these effects are usually associated with the excitation of SPPs. Planar metamaterials based on thin metal films are significantly easier to manufacture than three-dimensional ones and they also manifest a resonant optical response leading to various effects in the optical range. If a periodic array of subwavelength holes is created in a metal film with a thickness of several skin layers, the effect of extraordinary optical transmission (EOT) is observed—the transmitted electromagnetic wave intensity is drastically enhanced at the surface plasmon resonance wavelength in comparison to off-resonance frequencies [19].

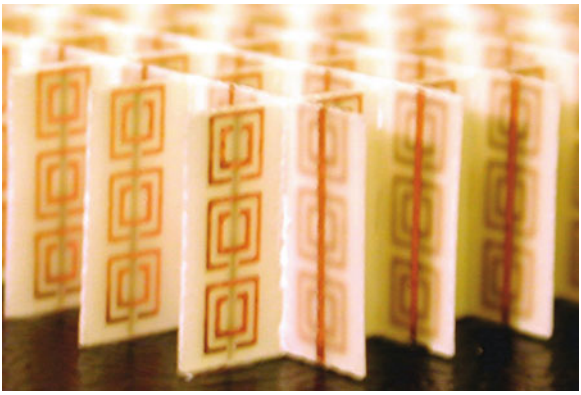

Fig. 2.7 The first experimentally demonstrated negative-index metamaterial. Split current rings induce effective negative permeability and straight vertical rods supply negative permittivity [21]

V.G. Veselago [20] suggested the existence of a hypothetical medium with simultaneously negative dielectric constant ε and magnetic permeability μ for the electromagnetic wave of a given frequency. The Maxwell's equations analysis shows that the wave propagating in a medium with negative $Re(\varepsilon)$ and $Re(\mu)$ has the opposite phase and group velocities, which suggests that the refractive index of such media is less than zero. Experimental confirmation of the existence of such media for electromagnetic waves of the radio frequencies [21] required the construction of an array of specially shaped objects (Fig. 2.7) that are resonant for both the electric and magnetic components of the electromagnetic wave. For the realization of media with negative refractive index at optical wavelengths, it is possible to use metals providing a negative real part of the refractive index. However, the bulk magnetization of the media at optical frequencies is close to zero for all known natural materials making the magnetic susceptibility of the latter close to unity. To achieve an effective magnetic response of the medium in the optical range—in other words, to observe the phenomenon of optical magnetism—the nanostructured media can be used, such as ordered arrays of metallic nanoparticles [22]. The electric component of the incident electromagnetic wave can excite both symmetric and antisymmetric oscillations in a pair of nanoparticles. The symmetric oscillations give a nonzero electric dipole moment of the system, while in the case of the antisymmetric resonance the electric dipole moment is close to zero but the counter-flowing "ring" currents yield a magnetic dipole moment emulating the magnetization of the medium. The effective value of the magnetic susceptibility can be different from unity, as well as negative value, which opens the way for the practical realization of materials with negative refractive index [18, 23].

Another anomaly was observed in optical metamaterials made of thin films perforated with an ordered array of subwavelength apertures. According to Bethe's model [24] of light transmission through the circular subwavelength aperture of radius r made in the thin conducting film, the transmission coefficient can be written as follows:

$$T(\lambda) = 64(kr)^4/27\pi^2, \tag{2.11}$$

where $k = 2\pi/\lambda$ is the wavenumber. Later on, it was shown [19] that the regular array of subwavelength apertures fabricated in non-transparent silver film and arranged with the minimal period of d possesses the transmission coefficient spectrum having peaks at the wavelengths corresponding to SPP resonances described by Eq. (2.10). The maximal value of transmission was shown to be approximately two orders of magnitude larger than that expected by Eq. (2.11). This phenomenon is now known as the extraordinary optical transmission effect since the total light transmission normalized at the aperture area appears to be larger than unity. One of the mechanisms responsible for electromagnetic energy transfer from one side of the nanoperforated metallic film to another one is the resonant SPP excitation at the film surface followed by penetration of SPP modes through the nanoholes and further coherent diffraction of SPP at the film backside into the propagating electromagnetic wave according to the phase matching conditions at the periodic array of nanoholes [25, 26].

One of the spectacular features of the EOT effect is the maintenance of spatial coherence of the collimated beam upon transmission through the nanohole array supported by recent experiments on entanglement of a biphoton as one of its parts was transmitted through the nanohole array [27]. Small losses of the entanglement show the quantum nature of the EOT phenomenon that allows consideration of SPP as quasiparticles with a lifetime inversely proportional to the spectral width of the SPP resonance.

The EOT effect possesses strong spectral selectivity for the incoming radiation since the spectral position of the EOT peak corresponds to the spectral line of the SPP excitation at the surface of the nanoperforated sample [3]. The spectral position of the EOT peak can be tuned by changing the geometrical parameters of the structure such as the nanoholes period, form and size of holes, and film thickness. Therefore, the optical properties of periodically modulated surfaces of noble metals are also defined by the effectiveness of the excitation of the SPP modes. However, since electromagnetic radiation induced by coherent SPP scattering at the spatially modulated surface can interfere with the incoming light exciting surface plasmons, the spectral lineshape of the response of such structures can significantly differ from the Lorentz lineshape.

The discovery of EOT [19] in 1998 yielded long and intensive debates of its nature and different interpretations of the effect. The main problem was that the calculated surface plasmon resonances did not coincide with experimental EOT peaks. The anomalous increase in transmission both of subwavelength hole arrays and gratings with narrow slits can be caused by the excitation of SPPs at the two interfaces of a film, as well as of the waveguide plasmon modes within the holes [28]. This interpretation was confirmed in further experiments: it was shown that the resonant transmission through a one-dimensional lattice of 60-nm-thick gold film can be caused by SPP excited at the upper interface only, as well as by localized waveguide modes [29]. On the other hand, Cao and colleagues have obtained a decrease in transmittance at the of SPP excitation wavelength for thicker films of 4 μm, and argued that the EOT arises only due to the localized waveguide modes [30]. Later, it was assumed that the localized plasmons at the holes play an

important role in EOT. A lot of different shapes of holes were considered and it was found that their shape and configuration are important for the fixed period [31]. The more complex is the shape of a hole, the easier nonpolarized light couples into its local mode. Moreover, the symmetry of two-dimensional lattices is important for transmittance value. For example, it was found that EOT was stronger for hexagonal lattice than that for square lattice [32]. Then it became clear that the excitation of SPP affects the resonance characteristics of localized plasmons. For example, if Wood's anomaly appears, the resonances of localized plasmons are red-shifted due to Fano-type interference. It was shown for very narrow slits (much less than the thickness of the film) that the resonance of SPP reduce the transmission. The situation can be completely different for slits width comparable to the period, because local modes inside the slits cannot be excited any more, while local plasma oscillations can appear within the stripes.

2.5 Optically Anisotropic Metamaterials: Versatile Polarization Control with Plasmonic Nanostructures

2.5.1 Far-Field Polarization Control

For changing the state of polarization (SoP) of light two key optical elements are commonly used, namely a polarizer and a wave plate. While polarizers are used to prepare the output SoP which does not depend on the input SoP, wave plates are used to transform the incident SoP. The principles of operation of a polarizer which prepares a linearly polarized state rely on the effect of linear dichroism under which only linearly polarized light is transmitted through and the orthogonal polarization is reflected, deflected, or absorbed. The wave plate introduces a phase delay between two orthogonal linear polarizations which are eigenpolarizations of the wave plate; as a result general elliptical polarization is the output from the device. Since there are two parameters defining any fully polarized SoP, i.e., the ellipticity E of the polarization ellipse and its major axis orientation with respect to the laboratory frame, φ, there are also two parameters which define the SoP output from any wave plate. These parameters are wave plate optical axis orientation angle ψ and the amount of phase delay introduced between the eigenpolarizations, $\Delta\phi$.

In comparison to the bulk polarization elements plasmonic nanostructures comprise materials of essentially subwavelength thicknesses. Thus the thickness cannot be continuously tuned to achieve the desired phase shift between the eigenpolarizations. Nevertheless plasmonic anisotropic nanostructures were proven to compete with the bulk polarization optics [33–37]. In this section we investigate what parameters could be tuned in order to attain the desired polarization state output from an anisotropic plasmonic nanostructure.

The sensitivity of SPPs to the polarization of light allows for the observation of linear birefringence and dichroism. Consider a metal surface that is modulated along

the Ox direction and radiation impinging on the surface at an angle θ in the plane of incidence parallel to Ox (Fig. 2.5). It is possible to excite an SPP according to phase-matching conditions (2.10) with the in-plane polarized light. A dip will be observable in reflection spectra corresponding to energy transfer from the incident wave to SPP. Light polarized perpendicularly to the plane of incidence (s-polarization) is not capable of SPP excitation and is reflected without significant losses. Due to symmetry restraints s- and p-polarized waves are eigenpolarizations of the grating since the polarization state is not changed by reflection. An SoP, which comprises a linear combination of these eigenstates, may undergo changes depending on so-called ellipsometric constants of the medium:

$$\xi = \left|\frac{r_p}{r_s}\right|, \quad \Delta\varphi = \varphi_p - \varphi_s, \tag{2.12}$$

where $r_{5p} = |r_p| \exp i\varphi_p$ and $r_s = |r_s| \exp i\varphi_s$ are field reflection coefficients of p- and s-polarized waves, respectively. Since the effectiveness of SPP excitation has strong dispersion, a pronounced spectral inhomogeneity is observed for ξ and $\Delta\varphi$.

Dispersion and, hence, polarization transformation performance depend on the parameters of the resonance. The spectral response of the most resonant physical systems is described by a Lorentzian line shape. The spectrum of a system response to harmonic excitation of frequency ω is described by a classical harmonic oscillator model:

$$T_L(\omega) = \frac{B}{\omega^2 - \omega_0^2 - 2i\gamma\omega}, \tag{2.13}$$

or with the assumption of $\omega_0 \gg \gamma$ for analytical signals :

$$T_L(\omega) = \frac{B}{\omega - \omega_0 - i\gamma}, \tag{2.14}$$

where B is the amplitude of the excitation, ω_0 the natural frequency of the oscillator, and γ the damping factor. However, the observed signal is often a mix of T_L and the exciting signal. In this case the spectral line becomes asymmetric of the Fano-type [7]:

$$T_F(\omega) = A + \frac{Be^{i\phi}}{\omega - \omega_0 - i\gamma}, \tag{2.15}$$

where A is the amplitude of nonresonant signal, and ϕ the phase between resonant and nonresonant signals. The shape of the Fano resonance is a common lineshape of the optical response spectra of nanostructured systems supporting the excitation and propagation of SPP. Thus, the transmittance spectra of thin films of metal with a periodically modulated surface contain Fano resonance features. This is the consequence of the fact that the reflected signal contains two coherent components: the

light transmitted through the film directly, and the radiation coupled into a surface mode and then diffracted in accordance with the phase-matching condition (2.10). Fano resonances in the optical response of nanostructures are attracting considerable interest due to their high spectral selectivity [3, 38].

By using a plasmonic nanostructure with a Fano resonance, one can attain high polarization conversion by means of plasmon-enhanced birefringence and dichroism [36]. One may use nanoslit arrays in a thin gold film to achieve a sharp Fano-type resonance for visible wavelengths. The transmission of such a sample is presented in Fig. 2.8a as a function of incident light's photon energy and wave vector projection onto a sample's plane k_x for the p-polarized light. A sharp and angle-dependent Fano-type resonance is observed in the visible range; a cross-section of the transmission function at the angle of incidence $\theta = 50°$ is shown in Fig. 2.8b. The origin of the Fano-type optical response lies in the coherent superposition of the grating SPPs resonance response and the background signal directly transmitted through the 30-nm-thick gold film. The phase delay $\Delta\varphi$ between E_y and E_x of the output E-field's components and the dichroism $|E_x|^2/|E_y|^2$ are measured in the spectral domain and shown in Fig. 2.9a for $\theta = 50°$. The phase difference varies from 0.38π to 0.85π, which could be obtained by a medium of the same thickness with extreme ordinary–extraordinary refractive indices differences of $\Delta n \simeq 4.4 - 10.4$.

Note that the spectral position of a feature in the $\Delta\varphi$ spectrum is connected to the position of the SPP resonance. It means that if one fixes the operating wavelength, there is a strong dependence of the phase delay on the angle of incidence. The phase delay could be tuned continuously within the aforementioned range of 0.38π–0.85π by varying the angle of incidence within the range of 46° to 54°. The angle of incidence stands as a birefringence control parameter—a substitute to the wave plate thickness in the bulk polarization optics.

2.5.2 Near-Field Polarization Control

Surface plasmon-polaritons being related to spatial electron plasma oscillations in a metal are strongly localized to nearby the metal surface. The characteristic scale of the localization of bounded electromagnetic waves depends on various factors such as the form of metallic objects and curvature of their elements and appears to be from several nanometers to subwavelength scale, which in a majority of cases is sufficiently lower than diffraction limit for the optical wavelength used. Concentration of electromagnetic energy in the objects with the a size smaller than the optical wavelength in vacuum, which is called subwavelength focusing or superfocusing, and optical signal transfer over subwavelength channels were experimentally demonstrated in various systems, for example, in individual nanoparticles [39], in nanoparticle chains [40, 41], in V-shaped subwavelength grooves fabricated at the smooth metallic surfaces [13], and at near-field optical microscopy probes [42], involving interference of standing plasmonic waves [43], utilizing radially [44] or

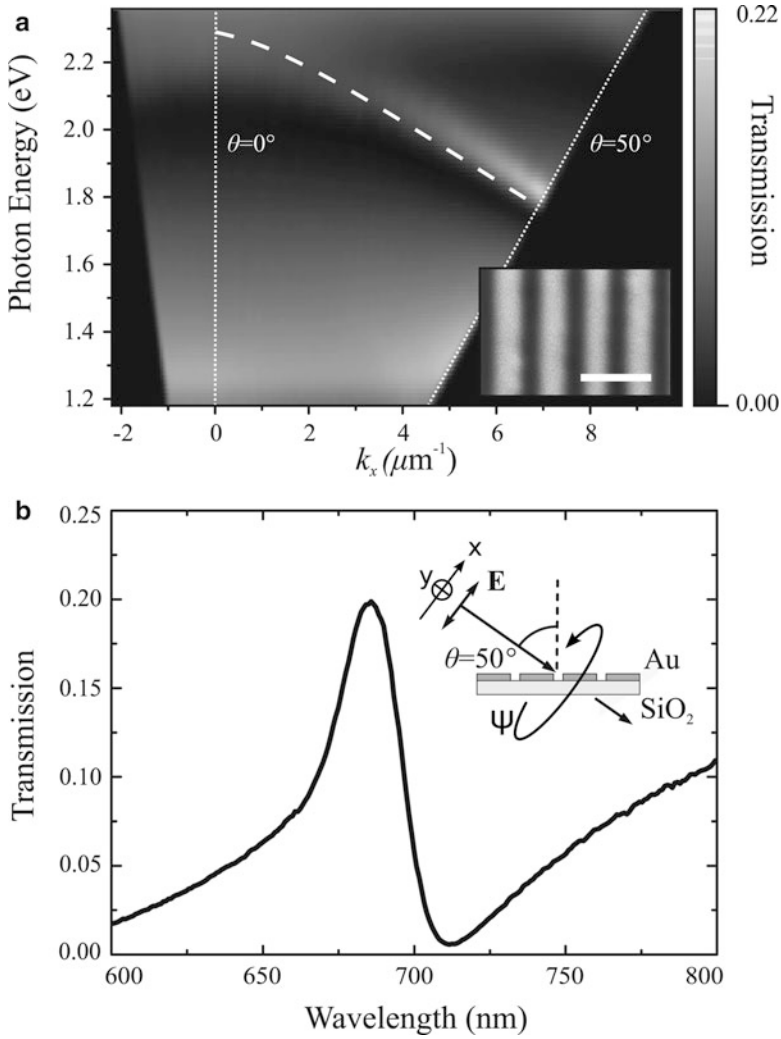

Fig. 2.8 (**a**) Transmission coefficient of the nanoslit sample as a function of photon energy and transversal wavenumber of the incident *p*-polarized light. SPP excited with the blazing − 1 diffraction order is present. The dispersion relation of SPP propagating at a gold-fused silica interface estimated using the expression (2.10) is denoted with the *white dashed line*. The inset shows the SEM picture of the sample, the bar length equals 500 nm. (**b**) The transmission spectrum at the 50°-incidence indicating a Fano-type resonance for the *p*-polarized light [37]

circularly [45] polarized beams. The practical realization of concentrating electromagnetic energy at the scale smaller than the optical wavelength in vacuum seems to be an important task towards miniaturization of optical devices such as nanolasers [46, 47] or elements for optical computing [48].

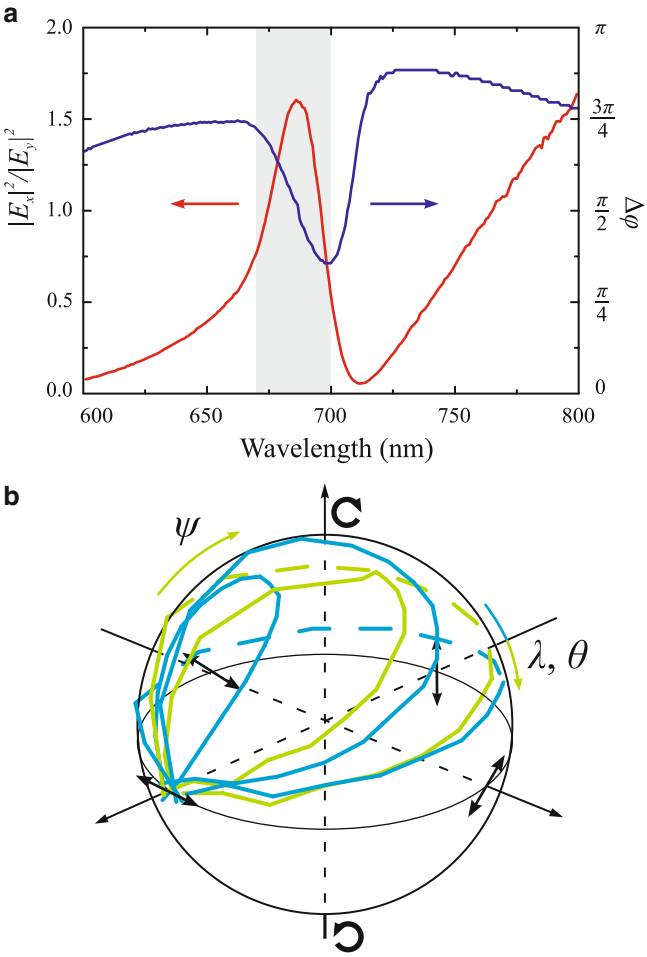

Fig. 2.9 (**a**) Linear birefringence and dichroism of the nanoslit sample represented by the phase retardation $\Delta\varphi$ and $|E_x|^2/|E_y|^2$ spectra, respectively, measured at the 50°-incidence. (**b**) The Poincaré sphere representing the map of experimental polarization transformations done by the system under study. The input state is horizontally polarized. Each curve describes a set of output states for azimuthal angle Ψ varying from 0° to 90°. Different curves stand for different wavelengths in the vicinity of Fano resonance or different angles of incidence, calculated using the $\partial\theta/\partial\lambda$ expression from the text. Although not indicated, the bottom hemisphere is covered in the same way with $-\Psi$ angles due to symmetry relations [37]

Using the fact of subwavelength electromagnetic energy localization with SPPs, we show that not only energy density but also polarization could be separated in space by plasmonic nanostructures. To do this we measure linear dichroism in the subwavelength vicinity of an anisotropic plasmonic nanostructures. The nanostructures under study comprise very long plasmonic nanoparticles with a local plasmon resonance with the central wavelength of 580 nm excited with the

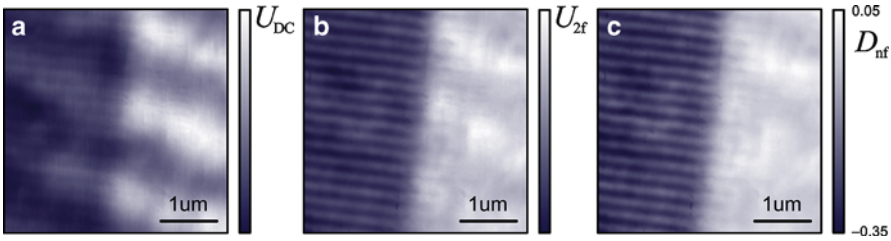

Fig. 2.10 (**a**) Distribution of U_{DC} in the subwavelength vicinity of the sample. (**b**) Distribution of U_{2f} in the subwavelength vicinity of the sample. (**c**) The ratio of the latter to the former showing the linear dichroism map

linear polarization perpendicular to the stripes. Near-field polarization properties of plasmonic nanogratings were investigated by means of scanning near-field dynamic polarimetry setup [49]. Horizontally polarized light from a doubled CW Nd:YAG laser with $\lambda = 532$ nm passes through a half-wave plate with its axis oriented at 22.5° with respect to the optical table. Diagonally polarized light passes through a photoelastic modulator (PEM) that temporally modulates the phase shift between vertically and horizontally polarized components. The phase shift undergoes harmonic oscillations $\phi(t) = A\sin(2\pi ft)$, where A is the phase shift oscillations amplitude and f is the PEM operating frequency which is equal to 47 kHz. If $A = \pi$ the polarization state output from the PEM changes from diagonal to antidiagonal with the $2f$ frequency. A half-wave plate placed behind the PEM is used for transformation of the polarization modulation from diagonal/antidiagonal to horizontal/vertical. Mirrors are used to deliver the light onto the sample through the substrate. Optical signal is then collected by an aperture SNOM fiber probe with the aperture diameter of 50–100 nm. The distance between the probe and the sample is about $\lambda/20$ and controlled by a three-coordinate piezo-driver. The collected signal is sent to a photomultiplier tube (PMT) and then divided into two channels. The first channel is connected to a lock-in amplifier which detects the signal modulation amplitude U_{2f} at the $2f$ frequency which is caused by the linear dichroism. The second channel is a low pass filter with the cutoff frequency of 600 Hz. Consequently both signals, U_{2f}, which is a measure of the linear dichroism, and U_{DC} which is proportional to transmittance, are simultaneously measured.

An example of the maps of U_{2f} and U_{DC} signals are given in Fig. 2.10a,b. Now obtaining the map of the absolute value of linear dichroism consists of dividing the former by latter [50, 51]. As a result we obtain a clear, speckle-free map of linear dichroism in Fig 2.10c which shows one how the polarization is distributed in the vicinity of the nanostructure. In other words, there are different places in the vicinity of the sample which are separated by a distance of 150 nm where light is polarized differently if the incident light state is not horizontally or vertically polarized one. While the mean dichroism value in the near-field regime -0.21 ± 0.03 coincides with one in the far field -0.20 ± 0.02, there is a subwavelength distribution of it in the plane of the sample.

2.6 Components of Nanoplasmonics for On-Chip Integration

In this section we examine the possibilities of creating basic components of the so-called plasmonic circuitry, which allow for plasmonic signal manipulation. The plasmonic circuit elements are divided into passive ones, which control the distribution of plasmonic energy corresponding to their shape, and active ones, which introduce the possibility of modulation of plasmonic signal by means of external electric or magnetic fields or electromagnetic radiation.

2.6.1 Passive Elements

The injection of surface plasmons onto the surface of a metallic film could be done by using methods described in Sect. 2.2. However, it is desirable to reduce the size of the photon-to-plasmon conversion terminal; for this, a single subwavelength defect in the surface of the film could be used. Figure 2.11 illustrates the distribution of the electromagnetic field density in the vicinity of the nanohole milled in a gold film illuminated with a monochromatic linearly polarized plane wave. Surface waves are seen spreading from the center of the aperture forming a dipole-like cosine-squared angular radiation pattern [52].

Figure 2.12 illustrates how an array of such apertures could be used as plasmonic field concentrators [53]. Each aperture is a point-like source of SPPs, which interfere in a preferential direction along the axis of mirror symmetry of the structure.

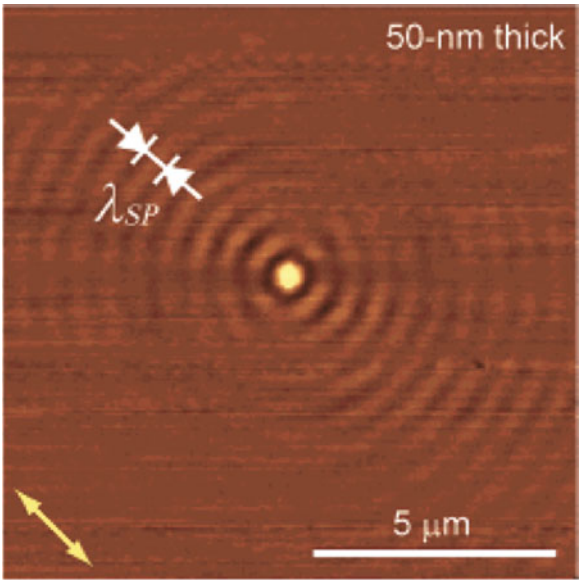

Fig. 2.11 The source of SPPs: electromagnetic field density in the vicinity of a 50-nm-thick golden film as measured with a SNOM. SPP Radiation pattern is seen with the main direction along the polarization of the incidence denoted with an *arrow* in the *bottom-left* part of the panel [52]

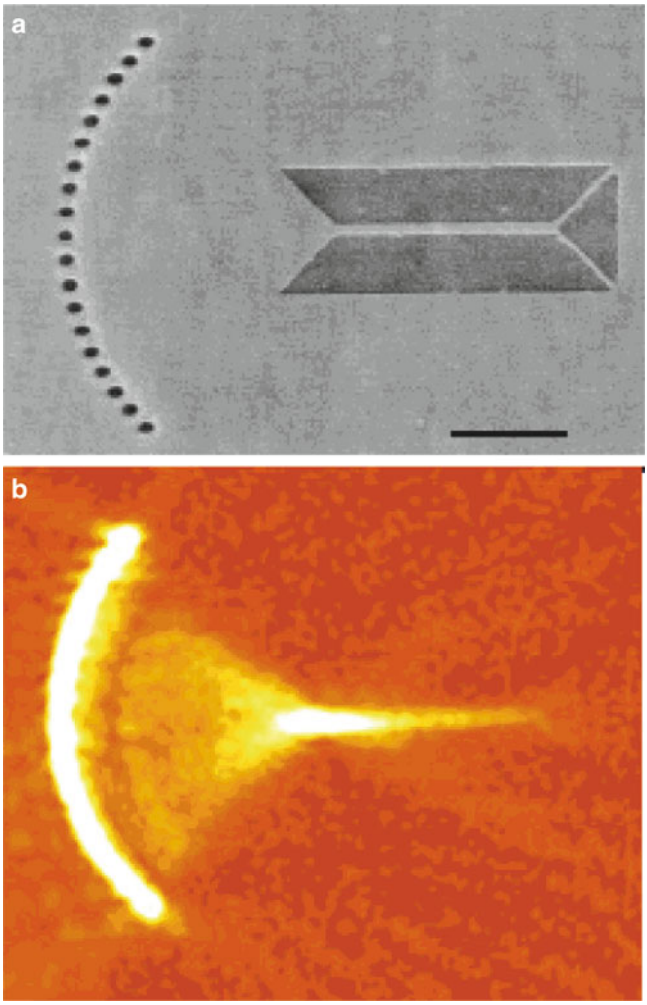

Fig. 2.12 Coupling of SPPs to waveguides. (**a**) An SEM image of an array of subwavelength apertures (*left*) and a ridge waveguide (*right*). (**b**) Focusing of plasmonic signal emitted from the apertures into the waveguide [53]

The result is a plasmon coupled to the bifurcation of the ridge waveguide with the width of 100 nm which scales as $\lambda/5$ at the wavelength used in the experiment.

The plasmonic hot spot in Fig. 2.12 is located at the beginning of a plasmonic waveguide that comprises a strip of gold along which SPPs can propagate. These so-called ridge waveguides allow for propagation of SPPs since SPP is a wave confined to the metal surface and follows the shape of it. However, SPPs undergo dramatic radiation losses in these waveguides since SPP is scattered by its edges. There are several possibilities to suppress these losses.

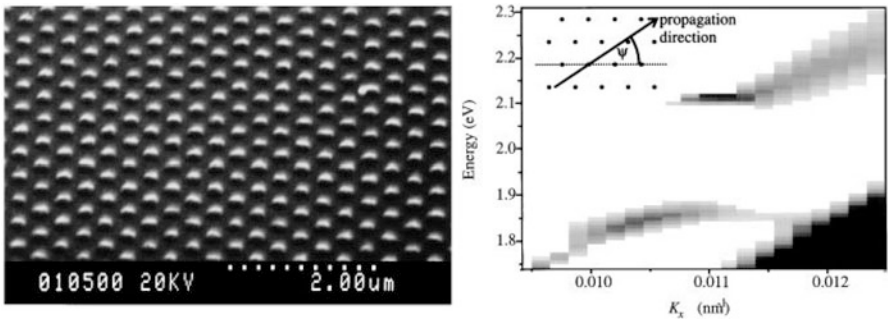

Fig. 2.13 *Left*: scanning electron micrograph of a plasmonic crystal surface. *Right*: visualization of the plasmonic band gap by measurement of the frequency and angular domain reflection spectra in the Kretschmann experimental geometry [54]

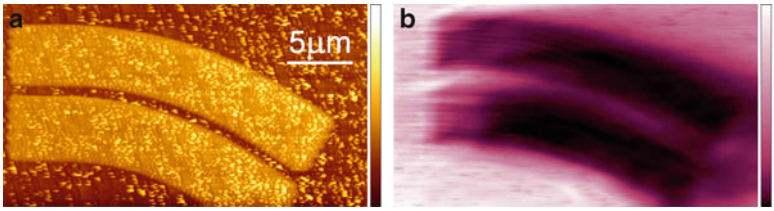

Fig. 2.14 SPPs in plasmonic crystal waveguides. (**a**) Topography of a plasmonic crystal-based bent waveguide. (**b**) SPP intensity distribution in the vicinity of the waveguide as measured by SNOM [55]

One of them is the usage of bandgap (BG) structures. A BG plasmonic structure is a periodically modulated metal-dielectric interface illustrated by the example of dielectric pillars on top of the metallic film in Fig. 2.13 [54]. When a plasmonic wave encounters such an array of scatterers, the secondary plasmonic waves may interfere in a way that no signal is transmitted through the BG structure. In this case a straight array of missed pillars acts as a waveguide for SPPs since the field in the areas of pillars tends to zero. The BG waveguides were demonstrated to guide SPPs along bent channels with low bending losses, as shown in Fig. 2.14.

The best plasmonic waveguide design in terms of low radiation losses is the so-called channel waveguides that represent a deep subwavelength groove in a metal film [13]. For the basic mode of the waveguide the SPP field is concentrated on the very end of the ditch making it hard to couple to the far-field and thus giving minor radiation losses as SPP is propagating along it. In Fig. 2.15c,d an experimental realization of such a waveguide is performed in a metal film. A 90° low-loss bend could be achieved by proper impedance matching of the waveguides it incorporates (Fig. 2.15a,b).

One can split one plasmonic wave into two or combine two of them into one by using a splitted waveguide as shown in Fig. 2.16. The topography of the surface of

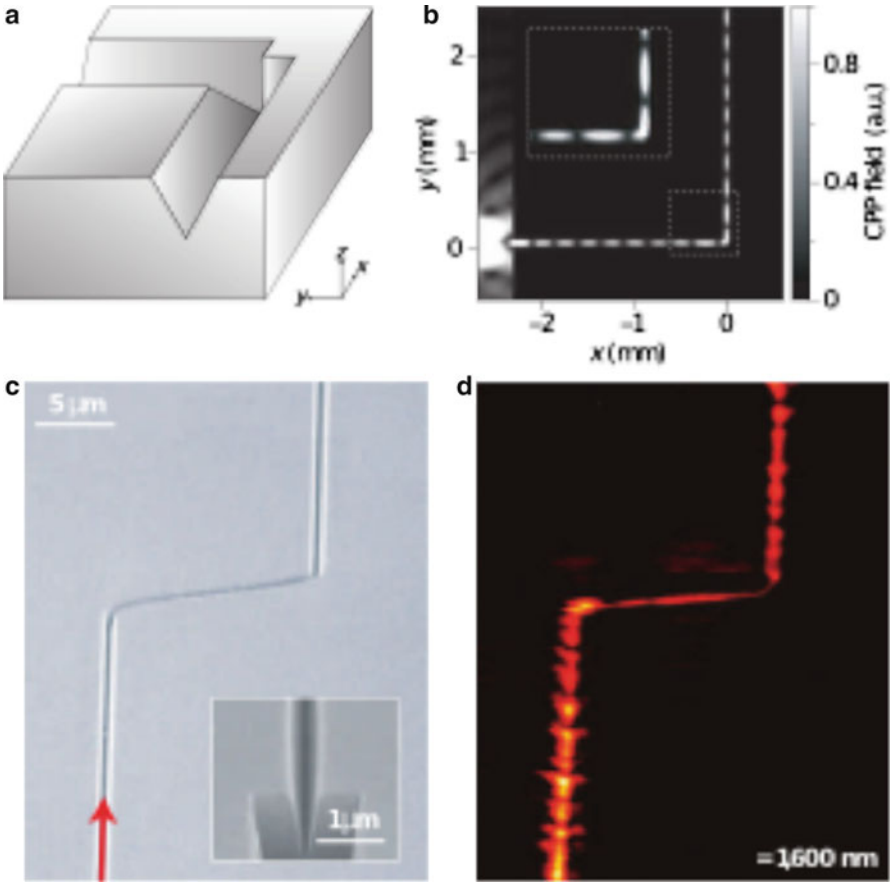

Fig. 2.15 SPPs in the V-groove waveguides. (**a**) Design of a 90°-bent channel plasmonic waveguide. (**b**) Results of calculation of the electromagnetic field intensity in the waveguide. (**c**) A scanning electron micrograph of a channel waveguide with a twist. (**d**) Respective SNOM image of SPP traveling along the waveguide [13]

the device is shown along with a near-field optical microscope image demonstrating field localization within the waveguide and its division over two plasmonic channels after the splitter.

Two plasmonic splitters could be combined into a Mach–Zehnder (MZ) interferometer. It has one input and one output; the intensity of the output signal depends on the phase of the waves which interfere within it. If one of the waves is retarded with respect to another by means of externally changing the local refractive index of gold or surrounding medium in one of the MZ arms, the output intensity would differ from one without this change. Thus the plasmonic output from such a device could be controlled via external stimuli allowing for modulation of the plasmonic signal for communication. So-called active ways of plasmonic signal creation and modulation are considered below.

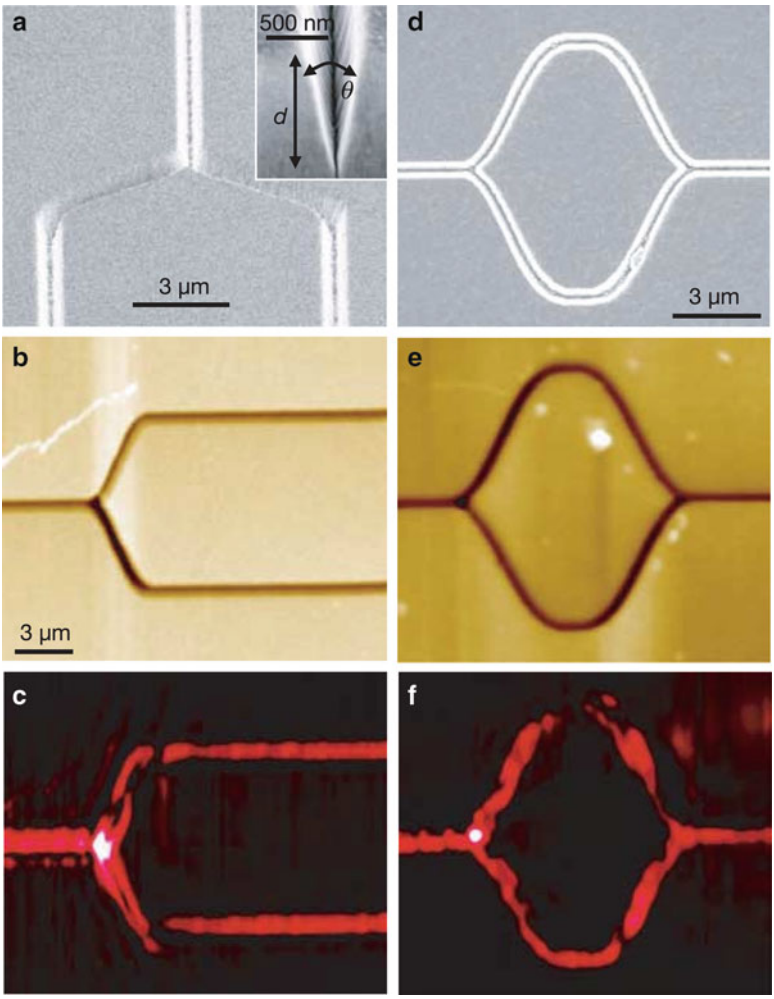

Fig. 2.16 (**a**)–(**c**) A channel-waveguide-based plasmonic splitter as viewed in a scanning electron microscope, atomic-force microscope, and SNOM. (**d**)–(**f**) A channel-waveguide-based plasmonic Mach–Zehnder interferometer as viewed in a scanning electron microscope, atomic-force microscope, and SNOM [13]

2.6.2 Active Elements

Like commercially available fiber-optic networks, every optical circuit requires a source of coherent radiation to be processed. Lasers are commonly used in optic networks; yet, the source of a coherent surface plasmon signal—a surface plasmon laser or a spaser—has been a long-standing problem for the community [47, 56–61]. The general idea of a spaser is depicted in Fig. 2.17. The active medium of a spaser is a luminescent substance—usually a dye or semiconductor quantum dots—that is placed in the near-field vicinity of a plasmonic nanoparticle, which

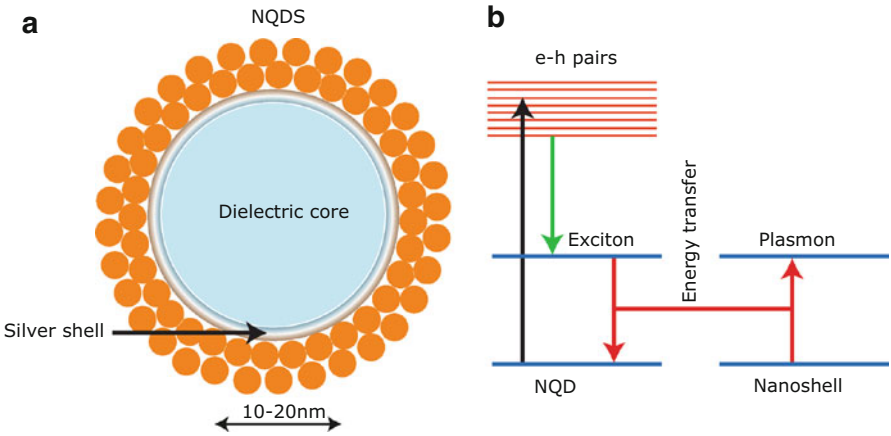

Fig. 2.17 A concept of a spaser. (**a**) A dielectriccore-shell dielectric-metal nanoparticle covered with nano quantum dots (NQDs). (**b**) Energy level diagram of the spaser. The *leftmost arrow* demonstrates the pumping of the NQDs with external radiation [56]

acts analogously to a cavity of a conventional laser. Luminescence is induced by optically pumping the active medium. After the pump power reaches certain critical value, the system starts to emit coherent surface plasmons within the spectral line of the nanoparticle's local plasmon resonance in the stimulated regime. Such a source could be placed inside a plasmonic waveguide since its dimensions are much smaller than a wavelength of an SPP.

An experimental verification of the possibility of a spaser was reported recently [57]. It was shown that a suspension of golden nanoparticles covered with a dye-doped silica shell demonstrates stimulated emission of photons in the far-field, which is a fingerprint of stimulated emission of SPPs in nanoparticles.

In order for information to be transferred via an SPP channel the latter should be modulated. Several methods of amplitude modulation of SPPs have been proposed. Applying an electric field could be used to modulate the SPP amplitude in a device called a metal-oxide-semiconductor field effect plasmonic modulator [48]. It consists of a multilayered structure with an optical source, a drain, and an electric gate (see Fig. 2.18). A surface plasmon mode is specific to an interface between metal and SiO_2 layers; an optical mode is specific to a Si waveguide; applying a gate voltage one sets the quality of the optical mode that may interfere with SPP giving rise to modulated transmission of the device as the gate voltage is modulated.

Another way is to control SPP by means of an optical signal, which is feasible for THz-clock systems. An example of ultrafast control over the SPP coupling to a gold film is demonstrated in a pump-probe experiment on plasmonic gratings [62]. Two sources of ultrashort laser pulses are used. The beam from the first one called the probe is coupled to the SPP mode by the grating coupling method described in Sect. 2.2. The other source provides a more powerful beam called the pump, which illuminates the sample and optically changes the dielectric properties of the dielectric surrounding the grating. Since the SPP resonance position strongly depends on

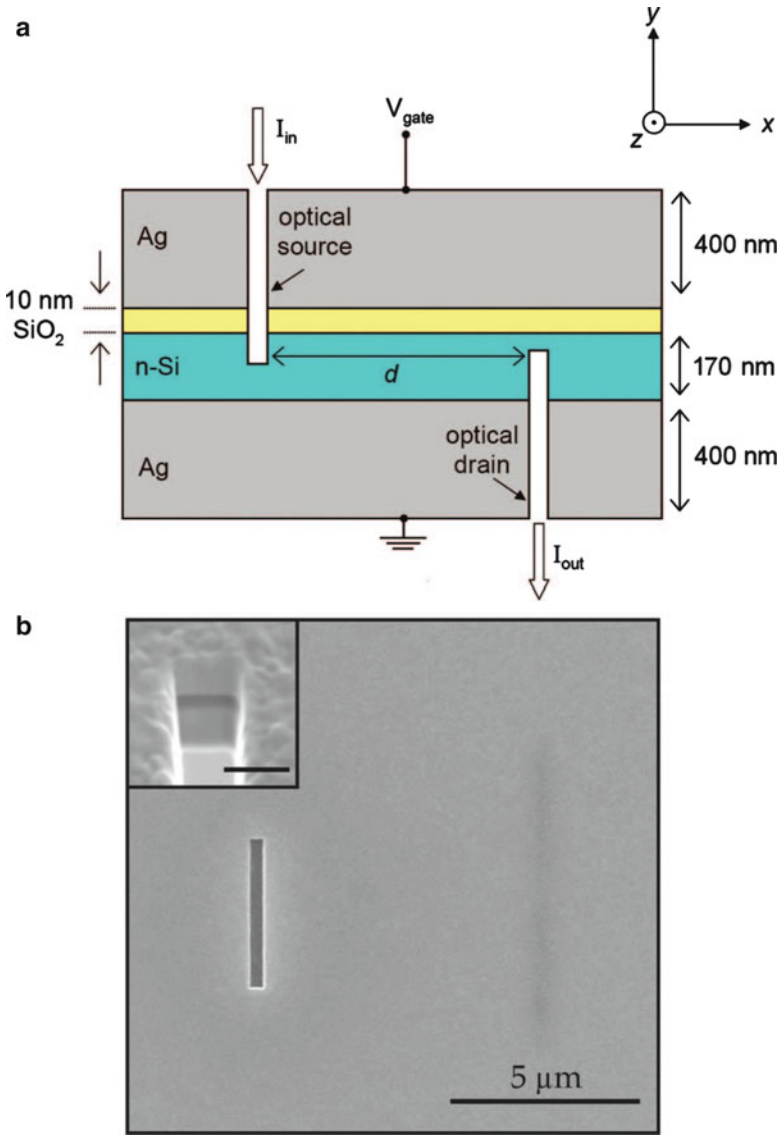

Fig. 2.18 (**a**) A schematic of a metal-oxide-semiconductor field effect plasmonic modulator. (**b**) A scanning electron microscope image of a prototype [48]

the dielectric properties of the surrounding medium [see Eq. (2.10)], even small changes of the dielectric permittivity of silicon induced by the carrier emission cause a spectral shift of the SPP resonance. Consequently, the SPP amplitude is diminished when the pump is present if the probe is at the SPP resonant wavelength in the unperturbed case. The speed of such switching lies at the sub-picosecond timescale, which paves the way for terahertz communications.

2.7 Ultrafast Nanoplasmonics

Nonequilibrium electron dynamics in metal nanoparticles and at plain and periodically perforated metal surfaces have been intensively studied during last decade using various femtosecond pump-probe and correlation spectroscopy techniques. The resonant enhancement of the transient thermoreflectance at unstructured surfaces due to surface plasmon excitation is shown to be a sensitive tool for time-resolved measurements of the metal surface temperature at the nanosecond [63] and subpicosecond [64] timescales. For the plane surfaces the SPP lifetime depends strongly on the metal optical constants and the surface roughness. The basic motivation of the studies of the SPP dynamics in nanostructures is the significant changes in the SPP relaxation times due to radiative damping suppression caused by the resonant excitation of the surface or localized plasmon modes. The ability to control these changes and to maximize the plasmon relaxation time for optical applications is an important motivation for this set of problems. For example, a significant reduction of both radiative and nonradiative plasmon damping was observed in gold nanorods in comparison to that in gold nanospheres of the similar sizes [65]. The resonance widths for individual particles of different sizes and shapes were measured. In the nanorods the damping is much slower and Q-factor is several times greater than that in the nanospheres. The observed difference is the strongest for the particles with red resonances, i.e., spheres with a larger size (high damping) and for nanorods with a larger length to diameter ratio (low damping). The local-plasmon dephasing times range from 1.4 to 5 fs for nanospheres and from 6 to 18 fs for nanorods as deduced from the experiment. The maximum dephasing time of 18 fs achieved for nanorods cannot be caused by changes in the radiative decay rate since its contribution is small for the small volume of particles. The reduced nonradiative decay in nanorods is explained by the fact that a threshold energy of about 1.8 eV in gold is higher than the resonant energy of the excited plasmons. For gold nanospheres this effect is screened by the strong radiative damping for the particular spectral region. Analysis of the results shows that contributions of radiative damping, interface damping, and pure dephasing to the process of dephasing are small in gold nanorods. The term "pure dephasing" means some additional elastic phase-loss process of the collective excitation.

The most appropriate technique for studying SPP dynamics is the optical femtosecond cross-correlation technique, which has many modifications. The common principle is the measurement of the correlation function (CF) of the reference femtosecond Gauss-shaped pulse and the pulse modified by the reflection from the studied object. The CF gives the time-resolved information of the processes occurring in the sample. The SPP relaxation processes described above depend strongly on the wavelength, thus a spectral modification of the cross-correlation techniques is required. A series of phase-sensitive correlation techniques is useful, such as frequency-resolved optical gating (FROG) and spectral interferometry. The methods give full parameters of the modified femtosecond pulse including the amplitude and phase of the electromagnetic field at any moment of time.

The metallic surface structuring allows the control of the surface plasmon lifetime for ultrafast plasmonics applications because SPP lifetime in plasmonic crystals can significantly vary depending on excitation and backscattering conditions (i.e., phase relations) as well as effective dispersion modification and photonic band gap presence within the spectral region of interest [66]. The strong distortion of a femtosecond pulse shape is reported in [67] due to resonant surface plasmon excitation in one-dimensional planar plasmonic crystal. The lifetimes of the SPPs excited on the lower and higher band gap edges differ as 18-fs at low-frequency band-gap edge and 250-fs at high-frequency band-gap. The competition of two relaxation channels gives rise to significant variations of the lifetime. The first channel is electron–electron and electron–phonon relaxation with the typical timescale similar to that at smooth surfaces. The second, which is much faster, is the radiative channel. Resulting lifetime value depends on the two channels' efficiencies ratio. The efficiency of the SPP reradiation in specular direction depends on the effective dispersion law slope and the SPP excitation method. The diffraction grating excitation method gives rise to the Wood's anomaly in the reflectance spectrum in the form of a Fano-type resonance. In this case, the radiation relaxation efficiency is strongly spectrally dependent on the vicinity of the resonance due to interference effects.

Pronounced light polarization conversion can be observed in thin metallic gratings due to strong optical anisotropy [37]. Moreover, the polarization conversion occurs at subpicosecond timescale, which was experimentally shown in [68] by using an original polarization-sensitive femtosecond correlation technique. One-dimensional plasmonic crystals were proposed as promising compact media for ultrafast polarization control as an application of the observed effect.

The ultrafast dephasing time of waveguide-plasmon polariton, which is a quasi-particle emerging due to strong coupling between the waveguide modes and the local plasmons, was studied in a 2D metallic photonic crystal structure with a nonlinear autocorrelation technique [69]. A phase-sensitive experimental setup with a stabilized Michelson interferometer and a 13-fs Ti:Sapp laser were used. A prolonged dephasing time of waveguide-plasmon polaritons is shown in metallic photonic crystals when compared to an undisturbed local plasmon. The experimental results demonstrate that it is possible to tailor the dephasing of the coherent excitation in metallic photonic crystals by tuning the coupling strength between the electronic and photonic resonances.

Coherent coupling between optical excitations can lead to a significant pulse propagation delay and a strong modification of the radiative damping rate [70–72]. By using an original time-resolved interferometric technique, a 6-fs delay of a 100-fs pulse transmitted through subwavelength hole arrays was observed [70]. The effective group velocity of $c/7$ of the pulse propagation through the media is measured. The experimental evidence of the subradiant damping in one-dimensional plasmonic crystal is given in [71]. The SPP lifetimes longer than 200 fs are demonstrated. Tuning of the SPP dephasing is demonstrated [73, 74]. In two-dimensional Au hole arrays, the reflectance linewidths decrease and the SPP lifetime increases with decreasing hole size and increasing wavelength [75].

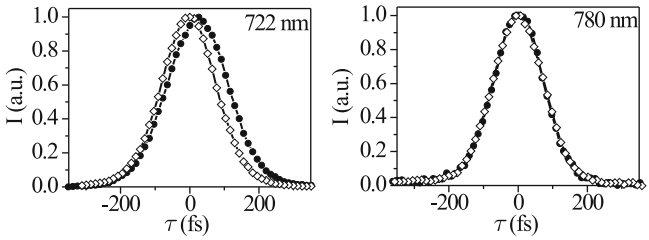

Fig. 2.19 Normalized second order intensity correlation function for *p*-polarization (*solid circles*) and *s*-polarization (*open circles*) at $\lambda = 722$ nm and $\lambda = 780$ nm [76]

A temporal modification of femtosecond pulses upon the resonant excitation of the SPPs was studied in one-dimensional metallic nanogratings by femtosecond correlation spectroscopy for the laser pulse duration comparable to the SPP lifetime [76]. The modification reveals itself as the time shift and pulse duration changes. Spectral dependence of the pulse distortion is described by the Fano resonance line shape. The grating was a 50-nm-thick silver film deposited onto a polymer substrate with a one-dimensional periodic surface topography modulation. The cross-section of the sample was close to a sinusoidal profile with the period of 750 nm and the modulation depth of 60 nm. Three resonances in the frequency-angular spectra were observed at three diffraction orders with $j = 1, \pm 2$, and ± 3 according to Eq. (2.10). The plasmonic origin of the resonance features observed in the vicinity of 500 nm and 725 nm was confirmed by the absence of such features in the s-polarized light reflectance. The interference of the reflected light and reradiated SPP yields Fano-shaped resonances (see Sect. 2.5). The spectral line shape of the reflectance is a sum of the nonresonant reflection of incident radiation and the resonance profile of SPP with the Lorentzian line shape as stated by Eq. (2.15). The SPP decay time calculated from the resonance width Γ is $t_{\mathrm{spp}} \simeq 90$ fs. The temporal modification of the femtosecond pulses was studied by the correlation spectroscopy. A Ti: sapphire laser with a pulse duration of approximately 200 fs, a repetition rate of 80 MHz, an average power of 100 mW, and the output wavelength tunable from 690 to 1,020 nm was used as a radiation source. The laser pulse was divided by the beam splitter into the reference and signal pulses. The reference pulse passed through the optical delay line. The signal pulse was reflected from the sample. Both beams were then focused on the nonlinear BBO crystal, and noncollinear second-harmonic generation was detected by a PMT. The angle of incidence of 67° was chosen to overlap the spectral range of the plasmon resonance with the laser tuning range. The experimental setup allowed for the measurements for both p- and s-polarized incident light. The dependence of the PMT signal on the delay time between pulses is the second order intensity correlation function (CF). The correlation function of the s-polarized pulse is an autocorrelation function since there is no excitation of SPPs and the laser pulse reflects from the sample without any perturbation. Measurements of CFs are performed in the spectral range from 710 to 800 nm.

Figure 2.19 shows the normalized correlation function measured for p- and s-polarized light at the resonant and nonresonant wavelengths of 722 nm

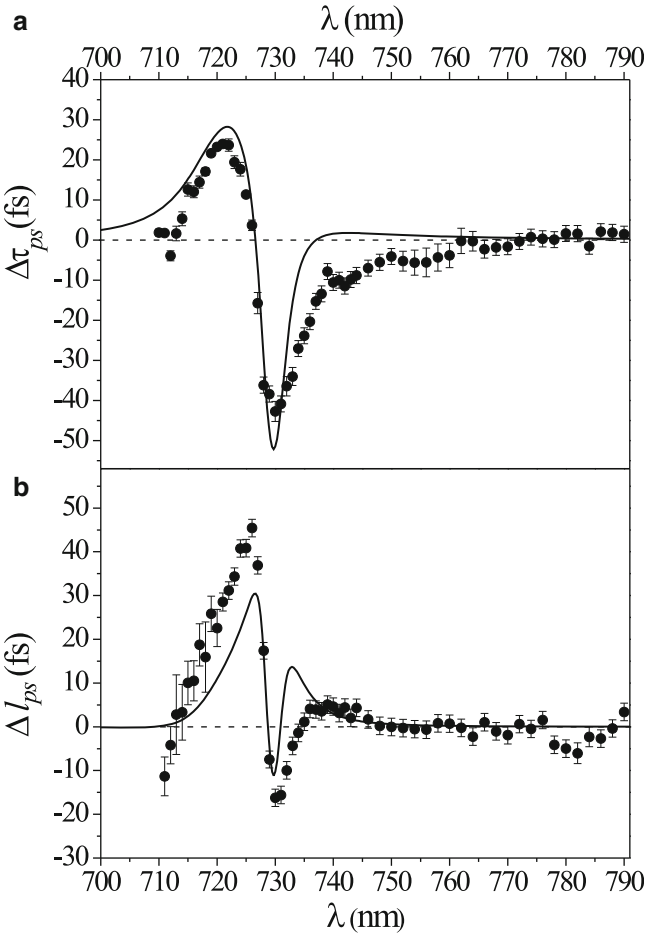

Fig. 2.20 The differential spectrum of the CF peak positions $\Delta\tau_{ps}$ (**a**) and the width of CF Δl_{ps} (**b**). The points stand for the experimental data, and the *solid curves* stand for the numerical calculations [76]

and 780 nm, respectively. The pronounced modification of the CF shape and shift of the CF maximum are observed in the vicinity of the resonance for the p-polarized pulses with respect to the s-polarized ones, while CFs for the p- and s-polarized pulses measured out of the resonance look similar. Figure 2.20a shows spectral dependence of the time shift between CF maxima for the p- and s-polarized pulses. The Fano-type interference gives the effect of both delay and leading of the p-polarized pulse relative to s-polarized pulse, as well as its broadening and narrowing in the vicinity of the resonance. The broadening of the CF measured for the p-polarized pulse and its delay in comparison to the nonresonant pulse is associated with the relaxation of resonantly excited SPPs. In the vicinity of the Fano

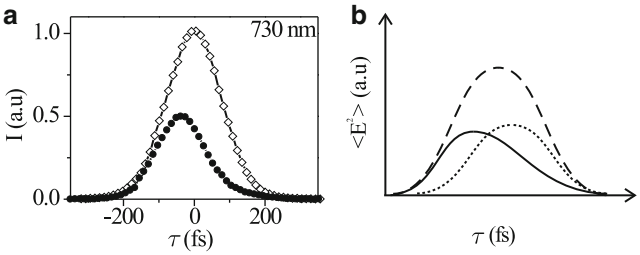

Fig. 2.21 (**a**) The second order intensity correlation function for *p*-polarized (*filled circles*) and *s*-polarized (*empty circles*) pulses at $\lambda = 730$ nm. (**b**) The schematic image of the destructive interference between the reflected pulse nonresonant component (*dashed line*) and delayed SPP excitation (*dotted line*). The *solid line* represents the resulting pulse reflected from the sample [76]

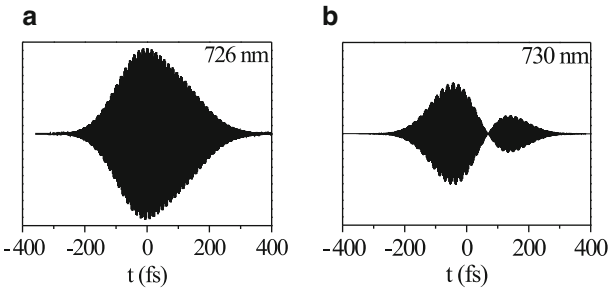

Fig. 2.22 The calculated time-dependent electric field of the pulse reflected from the sample. (**a**) Wavelength $\lambda = 726$ nm corresponds to the maximal CF broadening. (**b**) Wavelength $\lambda = 730$ nm corresponds to the minimum of the Fano resonance [76]

resonance minimum the CF amplitude measured for the p-polarized pulse and, consequently, the intensity of the pulse reflected from the sample is smaller than that of the s-polarized pulse as it is shown in Fig. 2.21a. The asymmetry of the CF shape and the CF maximum shift are clearly seen due to the destructive interference between the nonresonant and resonant reflected components of the p-polarized pulse as a result of an additional phase difference between them (Fig. 2.21b). If the pulse which is nonresonantly reflected from the sample is in phase with the pulse which is resonantly reemitted due to SPP excitation, they interfere constructively leading to the CF maximum shift to the positive time values and to the CF broadening. If the pulses interfere destructively, the CF peak shifts to the negative direction and the CF narrows.

Calculated spectral dependences of the CF shift and the CF width difference are shown by lines in Fig. 2.20. A good agreement with the experiments is seen. The result of the reconstruction of the electric field strength of the pulse reflected from the sample is shown in Fig. 2.22. The pulse is broadened in comparison to the reference pulse due to the SPP excitation 726 nm corresponding to the maximal CF broadening (Fig. 2.22a). Significant changes of the profile are also observed at the

Fano resonance minimum at 730 nm (Fig. 2.22b) due to the destructive interference. To conclude, the control over ultrafast optical response of plasmonic nanostructures can be attained for laser pulses duration comparable to the SPP lifetime.

2.8 Magnetoplasmonics

External magnetic field is prospective for fabrication of actively controlled plasmonic components which can be used in a wide number of applications. However, weak magneto-optical effects stemming from the weak spin-orbit interaction stimulate the search for the ways of enhancement of magneto-optical phenomena. One of the examples of photonic devices with magneto-optical response enhanced by proper nanostructuring is magnetophotonic crystals [77, 78] which are periodically structured magnetic dielectrics with the period comparable to the wavelength of the optical range. Last decade magnetophotonic crystals were in the focus of attention due to unique abilities of light propagation control they provide utilizing nonreciprocity of magneto-optical effects [79, 80]. In such structures significant Faraday angles and magneto-optical Kerr effect (MOKE) values were achieved [80–85]. Spatial localization of light was successfully used for enhancement of magnetic-field-induced nonlinear-optical response of magnetophotonic crystals [79, 81, 86–89]. Another approach for enhancement of magneto-optical response deals with periodically structured magnetic metallic materials, where propagating SPP can be excited due to the phase-matching between wave vectors of incident light and SPP and the vector of reciprocal lattice [90–96]. In analogy to magnetophotonic crystals, such materials can be considered as magnetoplasmonic crystals controlling SPP generation and propagation by periodicity.

Below we discuss briefly how longitudinal and transversal configurations of MOKE can be used for studying the spectral dependence of magneto-optical response enhancement at the Wood's anomaly of one- and two-dimensional (1D and 2D) magnetoplasmonic crystals based on nanostructured nickel films [92, 94–96]. Resonant excitation of SPPs leads to asymmetrical Fano-type spectral profiles of Kerr rotation and relative changes in reflectivity observed in the longitudinal and transversal magnetic field application, respectively. Such a lineshape was associated with Faraday and Voigt configurations of magnetoplasmon excitation at the surface of magnetoplasmonic crystals.

The atomic force microscopy and scanning electron microscopy images of the magnetoplasmonic crystal samples are shown in Fig. 2.23. The images show good lateral periodicity of both samples. The 1D magnetoplasmonic crystal sample was made by nanoimprint lithography in a 100-nm-thick nickel film forming a diffraction grating with a period of 320 nm and a modulation depth of 50 nm. The 2D magnetoplasmonic crystal consisted of a 2D hexagonal array of nickel nanodiscs with a height of 50 nm, a diameter of 200 nm, and a distance between centers of the neighboring discs of 400 nm.

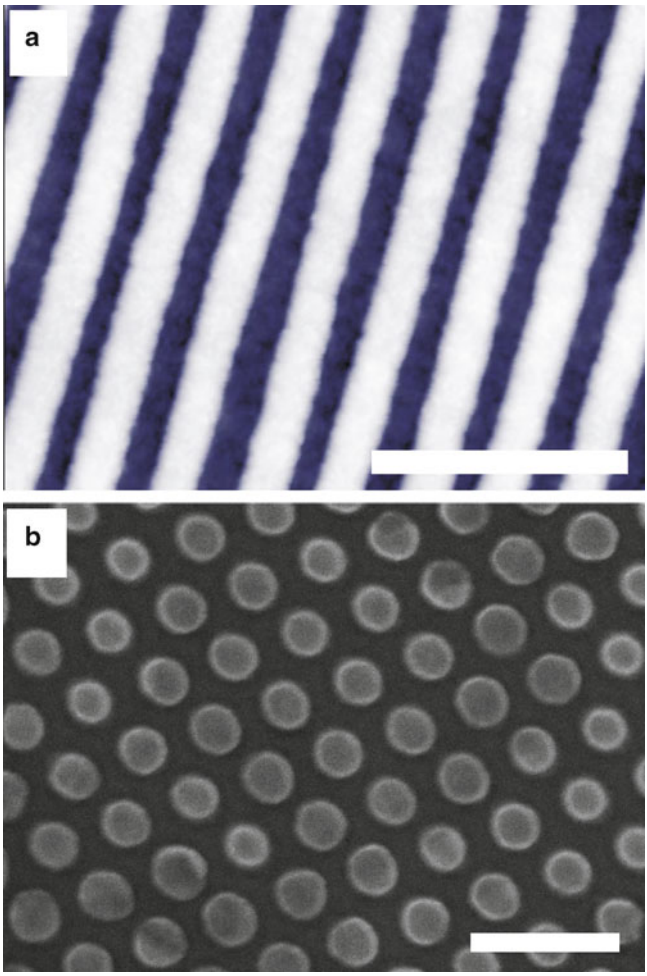

Fig. 2.23 (**a**) An atomic force microscopy image of the 1D magnetoplasmonic crystal sample. (**b**) A scanning electron microscopy image of the 2D magnetoplasmonic crystal sample. Scale bars in both images are equal to 1 μm

Two configurations of the external magnetic field application along the sample surface were used, namely the transversal one as magnetic field is perpendicular to the plane of incidence and the longitudinal one as the magnetic field is directed along the plane of incidence. The value of transversal magneto-optical Kerr effect (TMOKE) was defined as $\delta = (R(\mathbf{M}) - R(-\mathbf{M}))/R_0$, where $R(\mathbf{M})$, $R(-\mathbf{M})$, and R_0 are reflectance with and without the external magnetic field. Longitudinal magneto-optical Kerr effect (LMOKE) was characterized by the Kerr rotation angle of the linearly polarized radiation upon the reflection from the magnetized sample.

The spectral dependences of reflectance and TMOKE measured in the 1D magnetoplasmonic crystal are shown in Fig. 2.24.

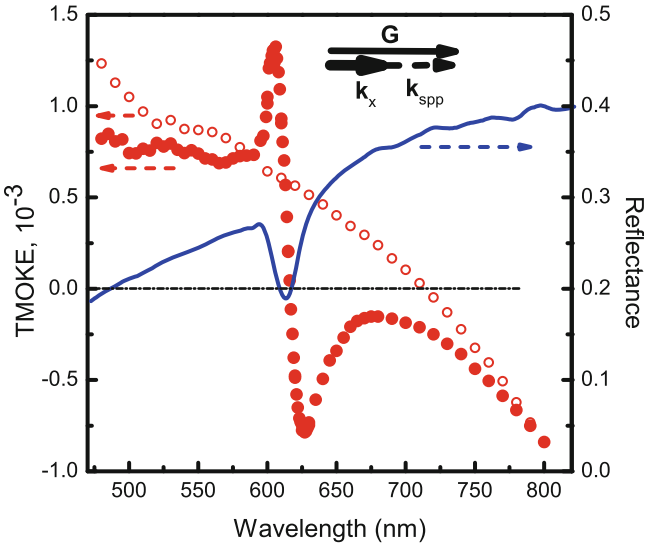

Fig. 2.24 TMOKE (*filled circles*) and reflectance (*curve*) spectra of 1D magnetoplasmonic crystal for the reciprocal vector oriented within the plane of light incidence. *Open circles*: TMOKE spectrum of 1D magnetoplasmonic crystal with the reciprocal vector perpendicular to the incident plane. Angle of incidence is 60°. *Inset*: schematic of the SPP phase-matching conditions with k_x is projection of the light wave vector onto the sample surface and k_{spp} is the SPP wave vector

Reflectance spectrum for p-polarized light measured in specular direction as the reciprocal vector **G** is oriented within the plane of incidence shows the fulfillment of the phase-matching conditions for the excitation of SPPs at the wavelength of 615 nm leading to a resonant dip associated with the Wood's anomaly. The spectral dependence of TMOKE value has a resonance in the vicinity of the Wood's anomaly with an asymmetric lineshape typical for the Fano-type resonance. The reference TMOKE spectrum measured for the sample azimuthal orientation as reciprocal vector is perpendicular to the incident plane providing the spectral behavior similar to that of a plain nickel film. The spectrum decays monotonously with the wavelength increase as it was expected for a nonstructured nickel surface.

The TMOKE is a result of the SPP dispersion curve shift upon the magnetization reversal at the surface of magnetoplasmonic crystals. The reflectivity minimum related to the Wood's anomaly is also spectrally shifted. Since the TMOKE value is proportional to the reflectivity difference for opposite magnetization directions, the spectral dependence of TMOKE has an asymmetric resonance lineshape. In the presence of the external magnetic field, SPPs have properties of magnetoplasmons [97] and TMOKE is related to the Voigt configuration of magnetoplasmons. Surface magnetoplasmon modes in the Voigt configuration are asymmetric with respect to the magnetization direction. The dispersion of SPPs reveals a magnetic-field-induced shift since the wave vector of magnetoplasmonic mode, k_{spp}^{M}, depends

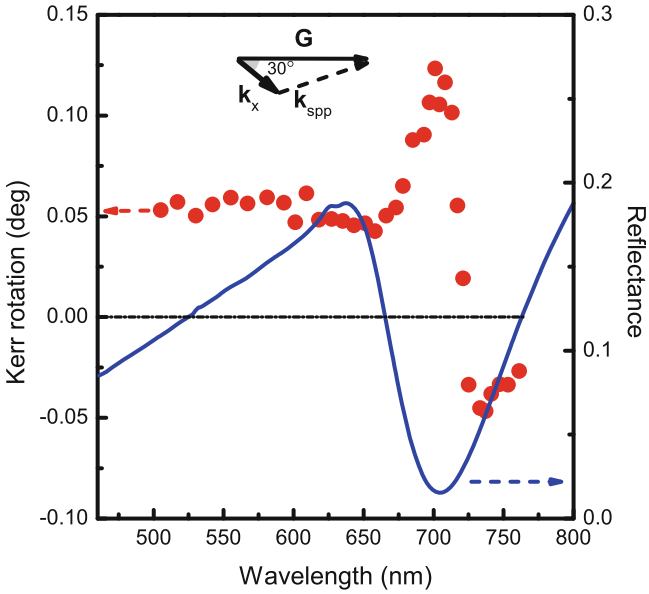

Fig. 2.25 The spectral dependences of the Kerr rotation angle in the longitudinal MOKE configuration (*circles*) and reflectance (*curve*) measured in the 2D magnetoplasmonic crystal. The angle of incidence is 45°. *Inset*: The schematic of the SPP phase-matching condition

on the value of the off-diagonal component of dielectric permittivity, g, in the following form [94, 95, 98]:

$$k_{spp}^{M} = k_{spp}\left(1 \pm \frac{g}{\xi}\right), \tag{2.16}$$

where

$$\xi = \sqrt{\varepsilon_0 \varepsilon_1}\left(1 - \frac{\varepsilon_0^2}{\varepsilon_1^2}\right), \; k_{spp} = \frac{\omega}{c}\sqrt{\frac{\varepsilon_0 \varepsilon_1}{\varepsilon_0 + \varepsilon_1}} \tag{2.17}$$

ε_0 is the dielectric permittivity of the space outside the magnetoplasmonic crystal and ε_1 is the diagonal component of the nickel dielectric permittivity. The phase matching conditions for the SPP excitation achieved for the opposite magnetization directions are fulfilled for different wavelengths resulting in an asymmetric TMOKE lineshape.

Figure 2.25 shows LMOKE spectrum measured in 2D magnetoplasmonic crystal. The sample was oriented exactly in between two adjacent reciprocal vectors of the hexagonal lattice so that the reciprocal vector **G** is oriented at 30° with respect to the plane of incidence as schematically shown in the inset of Fig. 2.25. The specular reflectance spectra for p-polarized light shows a Wood's anomaly at 700 nm. The Kerr rotation angle θ_K is enhanced up to 0.15° at the wavelength coinciding with the dip in the reflectance spectra and changes the sign upon spectral tuning across the Wood's anomaly.

LMOKE corresponds to the Faraday configuration of magnetoplasmonic modes excitation. In this case plasmonic wave contains both TM and TE components, and SPP can be represented as a coherent superposition of two components with right and left conical polarizations [94, 95]. Within the approximation, which is linearly dependent on g, the dispersion relation for these components is written as follows:

$$k_{spp}^{R(L)} = k_{spp}\left(1 \pm \frac{1}{2}\frac{\varepsilon_0}{(\varepsilon_0 + \varepsilon_1)\varepsilon_1} g\right). \tag{2.18}$$

The total amplitude of the SPP is determined by the coherent sum of these components, and the SPP polarization is defined by the phase shift between them. The asymmetric lineshape of the Kerr rotation spectra at the Wood's anomaly is attributed to slightly different phase-matching conditions for SPP modes with the wave vectors $k_{\mathrm{spp}}{}^{R}$ and $k_{\mathrm{spp}}{}^{L}$.

Summarizing, spectral dependences of transversal and longitudinal magneto-optical Kerr effects measured in one- and two-dimensional magnetoplasmonic crystals possesses a resonant Fano-type enhancement in the angular and wavelength vicinity of the Wood's anomaly, which is associated with the phase-matched excitation of the magnetoplasmon modes excited in Voigt and Faraday configurations, respectively. One-dimensional perturbation of the magnetic metal surface leads to the pronounced resonances in the magneto-optical Kerr effects, while two-dimensional periodicity gives one the possibility for the spectral tuning of the SPP phase-matching conditions by using the superposition of two reciprocal vectors.

2.9 Conclusions

With many problems yet unsolved nanoplasmonics has already proven to be a highly promising area of photonics both from fundamental research and applications point of view. Surface plasmons reveal ways of subwavelength light localization and transport and allow of engineering of novel materials that are capable of efficient control over properties of light by means of optical anisotropy and magneto-optic effects.

Acknowledgements Authors would like to thank A.A. Ezhov, A.V. Chetvertukhin, A.A. Grunin, P.P Vabishchevich, and B.B. Tsema for fruitful discussions.

References

1. V.M. Agranovich, D.L. Mills, *Surface Polaritons - Electromagnetic Waves at Surfaces and Interfaces* (Elsevier Science, New York, 1982)
2. H. Raether, *Surface-Plasmons on Smooth and Rough Surfaces and on Gratings* (Springer, Berlin, 1988)

3. W.L. Barnes, J. Opt. A Pure App. Opt. **8**(4, Sp. Iss. SI), S87 (2006)
4. H.C. van de Hulst, *Light Scattering by Small Particles* (Dover, New York, 1981)
5. K. Kelly, E. Coronado, L. Zhao, G. Schatz, J. Phys. Chem. B **107**(3), 668 (2003)
6. R.W. Wood, Philos. Mag. **4**(19–24), 396 (1902)
7. U. Fano, Phys. Rev. **124**(6), 1866 (1961)
8. A. Drezet, A. Hohenau, D. Koller, A. Stepanov, H. Ditlbacher, B. Steinberger, F.R. Aussenegg, A. Leitner, J.R. Krenn, Mat. Sci. Eng. B **149**(3), 220 (2008)
9. J.A. Veerman, A.M. Otter, L. Kuipers, N.F. van Hulst, Appl. Phys. Lett. **72**, 3115 (1998.)
10. R.J. Moerland, N.F. van Hulst, H. Gersen, L. Kuipers, Opt. Express **13**, 1604 (2005)
11. O. Marti, H. Bielefeldt, B. Hecht, S. Herminghaus, P. Leiderer, J. Mlynek, Opt. Commun. **96**, 225 (1993)
12. M. Balistreri, H. Gersen, J. Korterik, L. Kuipers, N. van Hulst, Science **294**(5544), 1080 (2001)
13. D.K. Gramotnev, S.I. Bozhevolnyi, Nat. Photonics **4**(2), 83 (2010)
14. S. Bozhevolnyi, V. Volkov, E. Devaux, J. Laluet, T. Ebbesen, Nature **440**(7083), 508 (2006)
15. S. Bozhevolnyi, J. Erland, K. Leosson, P. Skovgaard, J. Hvam, Phys. Rev. Lett. **86**(14), 3008 (2001)
16. A. Ezhov, S. Magnitskii, N. Maslova, D. Muzychenko, A. Nikulin, V. Panov, JETP Lett. **82**, 599 (2005)
17. R. Zia, M.L. Brongersma, Nat. Nanotechnol. **2**, 426 (2007)
18. V.M. Shalaev, Nat. Photonics **1**(1), 41 (2007)
19. T.W. Ebbesen, H.J. Lezec, H.F. Ghaemi, T. Thio, P.A. Wolff, Nature **391**, 667 (1998)
20. V.G. Veselago, Sov. Phys. Uspekhi **10**, 509 (1968)
21. R.A. Shelby, D.R. Smith, S. Schultz, Science **292**(5514), 77 (2001)
22. A.N. Grigorenko, A.K. Geim, H.F. Gleeson, Y. Zhang, A.A. Firsov, I.Y. Khrushchev, J. Petrovic, Nature **438**(7066), 335 (2005)
23. V. Shalaev, W. Cai, U. Chettiar, H. Yuan, A. Sarychev, V. Drachev, A. Kildishev, Opt. Lett. **30**(24), 3356 (2005)
24. H.A. Bethe, Phys. Rev. **66**(7-8), 163 (1944)
25. F.J. Garcia-Vidal, F. Lopez-Tejeira, J. Bravo-Abad, L. Martin-Moreno, *Surface Plasmon Nanophotonics* (Springer, New York, 2007)
26. H.F. Ghaemi, T. Thio, D.E. Grupp, T.W. Ebbesen, H.J. Lezec, Phys. Rev. B **58**(11), 6779 (1998)
27. E. Altewischer, C. Genet, M.P. van Exter, J.P. Woerdman, P.F.A. Alkemade, A. van Zuuk, E. W.J.M. van der Drift, Opt. Lett. **30**(1), 90 (2005)
28. J. Porto, F. García-Vidal, J. Pendry, Phys. Rev. Lett. **83**(14), 2845 (1999)
29. A. Barbara, P. Quémerais, E. Bustarret, T. Lopez-Rios, Phys. Rev. B **66**(16), 161403 (2002)
30. Q. Cao, P. Lalanne, Phys. Rev. Lett. **88**(5), 3 (2002)
31. P. Lalanne, J.C. Rodier, J.P. Hugonin, J. Opt. A **7**(8), 422 (2005)
32. Q.J. Wang, J.Q. Li, C.P. Huang, C. Zhang, Y.Y. Zhu, Appl. Phys. Lett. **87**(9), 091105 (2005)
33. R. Gordon, A. Brolo, A. McKinnon, A. Rajora, B. Leathem, K. Kavanagh, Phys. Rev. Lett. **92**(3), 037401 (2004)
34. S.Y. Hsu, K.L. Lee, E.H. Lin, M.C. Lee, P.K. Wei, Appl. Phys. Lett. **95**(1), 013105 (2009)
35. Y. Pang, R. Gordon, Opt. Express **17**(4), 2871 (2009)
36. M.R. Shcherbakov, P.P. Vabishchevich, M.I. Dobynde, T.V. Dolgova, A.S. Sigov, C.M. Wang, D.P. Tsai, A.A. Fedyanin, JETP Lett. **90**, 433 (2009)
37. M.R. Shcherbakov, M.I. Dobynde, T.V. Dolgova, D.P. Tsai, A.A. Fedyanin, Phys. Rev. B. **82**, 193402 (2010)
38. B. Luk'yanchuk, N.I. Zheludev, S.A. Maier, N.J. Halas, P. Nordlander, H. Giessen, C.T. Chong, Nat. Mat. **9**(9), 707 (2010)
39. R. Vogelgesang, A. Dmitriev, Analyst **135**, 1175 (2010)
40. C. Girard, Rep. Progr. Phys. **68**, 1883 (2005)
41. M. Salerno, J. Krenn, A. Hohenau, H. Ditlbacher, G. Schider, A. Leitner, F. Aussenegg, Opt. Commun. **248**(4-6), 543 (2005)

42. N.C. Lindquist, P. Nagpal, A. Lesuffleur, D.J. Norris, S.H. Oh, Nano Lett. **10**, 1369 (2010)
43. Q. Wang, J. Bu, X.C. Yuan, Opt. Express **18**(3), 2662 (2010)
44. G.M. Lerman, A. Yanai, U. Levy, Nano Lett. **9**(5), 2139 (2009)
45. W. Chen, D.C. Abeysinghe, R.L. Nelson, Q. Zhan, Nano Lett. **10**(6), 2075 (2010)
46. D. Bergman, M. Stockman, Phys. Rev. Lett. **90**(2), 027402 (2003)
47. R.F. Oulton, V.J. Sorger, T. Zentgraf, R.M. Ma, C. Gladden, L. Dai, G. Bartal, X. Zhang, Nature **461**(7264), 629 (2009)
48. J.A. Dionne, K. Diest, L.A. Sweatlock, H.A. Atwater, Nano Lett. **9**(2), 897 (2009)
49. E.B. McDaniel, S.C. McClain, J.W.P. Hsu, Appl. Opt. **37**(1), 84 (1998)
50. M.R. Shcherbakov, B.B. Tsema, Y.B. Tsema, A.A. Ezhov, V.I. Panov, D.P. Tsai, A.A. Fedyanin, Physica C **479**, 183 (2012)
51. M. Shcherbakov, B. Tsema, A. Ezhov, V. Panov, A. Fedyanin, JETP Lett. **93**, 720 (2011)
52. H. Gao, J. Henzie, T.W. Odom, Nano Lett. **6**(9), 2104 (2006)
53. L. Yin, V.K. Vlasko-Vlasov, J. Pearson, J.M. Hiller, J. Hua, U. Welp, D.E. Brown, C.W. Kimball, Nano Lett. **5**(7), 1399 (2005)
54. S. Kitson, W. Barnes, J. Sambles, Phys. Rev. Lett. **77**(13), 2670 (1996)
55. I. Radko, T. Sondergaard, S. Bozhevolnyi, Opt. Express **14**(9), 4107 (2006)
56. M.I. Stockman, Nat. Photonics **2**(6), 327 (2008)
57. M.A. Noginov, G. Zhu, A.M. Belgrave, R. Bakker, V.M. Shalaev, E.E. Narimanov, S. Stout, E. Herz, T. Suteewong, U. Wiesner, Nature **460**(7259), 1110 (2009)
58. M. Noginov, G. Zhu, M. Mayy, B. Ritzo, N. Noginova, V. Podolskiy, Phys. Rev. Lett. **101**(22), 226806 (2008)
59. E. Plum, V.A. Fedotov, P. Kuo, D.P. Tsai, N.I. Zheludev, Opt. Express **17**(10), 8548 (2009)
60. J. Seidel, S. Grafström, L. Eng, Phys. Rev. Lett. **94**(17), 177401 (2005)
61. N.I. Zheludev, S.L. Prosvirnin, N. Papasimakis, V.A. Fedotov, Nat. Photonics **2**(6), 351 (2008)
62. J.N. Caspers, N. Rotenberg, H.M. van Driel, Opt. Express **18**(19), 19761 (2010)
63. S. Herminghaus, P. Leiderer, Appl. Phys. A Mater. Sci. Process. **51**(4), 350 (1990)
64. R.H.M. Groeneveld, R. Sprik, A. Lagendijk, Phys. Rev. Lett. **64**, 784 (1990)
65. C. Sönnichsen, T. Franzl, T. Wilk, G. von Plessen, J. Feldmann, Phys. Rev. Lett. **88**(7), 077402 (2002)
66. D. Kim, S. Hohng, V. Malyarchuk, Y. Yoon, Y. Ahn, K. Yee, J. Park, J. Kim, Q. Park, C. Lienau, Phys. Rev. Lett. **91**(14), 143901 (2003)
67. A.S. Vengurlekar, A.V. Gopal, T. Ishihara, Appl. Phys. Lett. **89**(18), 181927 (2006)
68. M.R. Shcherbakov, P.P. Vabishchevich, V.V. Komarova, T.V. Dolgova, A.A. Fedyanin, Phys. Rev. Lett. **108**, 253903 (2012)
69. T. Zentgraf, A. Christ, J. Kuhl, H. Giessen, Phys. Rev. Lett. **93**(24), 243901 (2004)
70. A. Dogariu, T. Thio, L.J. Wang, T.W. Ebbesen, H.J. Lezec, Opt. Lett. **26**(7), 450 (2001)
71. C. Ropers, D. Park, G. Stibenz, G. Steinmeyer, J. Kim, D. Kim, C. Lienau, Phys. Rev. Lett. **94**(11), 113901 (2005)
72. H. Su, Z. Hang, Z. Marcet, H. Chan, C. Chan, K. Wong, Phys. Rev. B **83**(24), 245449 (2011)
73. C. Ropers, G. Stibenz, G. Steinmeyer, R. Müller, D. Park, K. Lee, J. Kihm, J. Kim, Q. Park, D. Kim, C. Lienau, Appl. Phys. B **84**(1-2), 183 (2006)
74. T. Utikal, T. Zentgraf, J. Kuhl, H. Giessen, Phys. Rev. B **76**(24), 245107 (2007)
75. J. Li, H. Iu, D.Y. Lei, J.T.K. Wan, J.B. Xu, H.P. Ho, M.Y. Waye, H.C. Ong, Appl. Phys. Lett. **94**(18), 183112 (2009)
76. P.P. Vabishchevich, V.O. Bessonov, F.Y. Sychev, M.R. Shcherbakov, T.V. Dolgova, A.A. Fedyanin, JETP Lett. **92**(9), 575 (2011)
77. M. Inoue, K. Arai, T. Fujii, M. Abe, J. Appl. Phys. **85**, 5768 (1999)
78. M. Inoue, R. Fujikawa, A. Baryshev, A. Khanikaev, P. Lim, H. Uchida, O.A. Aktsipetrov, A. A. Fedyanin, T.V. Murzina, A.B.. Granovsky, J. Phys. D Appl. Phys. **39**, R151 (2006)
79. A.A. Fedyanin, T. Yoshida, K. Nishimura, G. Marowsky, M. Inoue, O.A. Aktsipetrov, JETP Lett. **76**, 527 (2002)
80. S. Kahl, A. Grishin, Appl. Phys. Lett. **84**, 1438 (2004)

81. A.A. Fedyanin, T. Yoshida, K. Nishimura, G. Marowsky, M. Inoue, O.A. Aktsipetrov, J. Magn. Magn. Mater. **258–259**, 96 (2003)
82. A.A. Fedyanin, O.A. Aktsipetrov, D. Kobayashi, K. Nishimura, H. Uchida, M. Inoue, J. Magn. Magn. Mater. **282**, 256 (2004)
83. R. Li, M. Levy, Appl. Phys. Lett. **86**, 251102 (2005)
84. A.G. Zhdanov, A.V. Fedyanin, O.A. Aktsipetrov, D. Kobayashi, H. Uchida, M. Inoue, J. Magn. Magn. Mater. **300**, e253 (2006)
85. A.B.. Khanikaev, A.V. Baryshev, P.B. Lim, H. Uchida, M. Inoue, A.G. Zhdanov, A.A. Fedyanin, A.I. Maydykovskiy, O.A. Aktsipetrov, Phys. Rev. B **78**, 193102 (2008)
86. T.V. Dolgova, A.A. Fedyanin, O.A. Aktsipetrov, K. Nishimura, H. Uchida, M. Inoue, J. Appl. Phys. **95**, 7330 (2004)
87. T.V. Murzina, R. Kapra, T.V. Dolgova, A.A. Fedyanin, O.A. Aktsipetrov, K. Nishimura, H. Uchida, M. Inoue, Phys. Rev. B **70**, 012407 (2004)
88. O.A. Aktsipetrov, T.V. Dolgova, A.A. Fedyanin, R. Kapra, T.V. Murzina, K. Nishimura, H. Uchida, M. Inoue, Laser Phys. **14**, 685 (2004)
89. O.A. Aktsipetrov, T.V. Dolgova, A.A. Fedyanin, T.V. Murzina, M. Inoue, K. Nishimura, H. Uchida, J. Opt. Soc. Am. B **22**, 176 (2005)
90. A.B.. Khanikaev, A.V. Baryshev, A.A. Fedyanin, A.B.. Granovsky, M. Inoue, Opt. Express **15**, 6612 (2007)
91. C. Clavero, K. Yang, J. Skuza, R. Lukaszew, Opt. Lett. **35**, 1557 (2010)
92. A.A. Grunin, A.G. Zhdanov, A.A. Ezhov, E.A. Ganshina, A.A. Fedyanin, Appl. Phys. Lett. **97**, 261908 (2010)
93. V.I. Belotelov, I.A. Akimov, M. Pohl, V.A. Kotov, S. Kasture, A.S. Vengurlekar, A. Gopal, D. Yakovlev, A. Zvezdin, M. Bayer, Nat. Nanotechnol. **6**, 370 (2011)
94. A.V. Chetvertukhin, A.V. Baryshev, H. Uchida, M. Inoue, A.A. Fedyanin, J. Appl. Phys. **111**, 07A946 (2012)
95. A.V. Chetvertukhin, A.A. Grunin, A.V. Baryshev, T.V Dolgova, H. Uchida, M. Inoue, A.A. Fedyanin, J. Magn. Magn. Mater. **324**, 3516 (2012)
96. A.A. Grunin, N. Sapoletova, K. Napolskii, A. Eliseev, A.A. Fedyanin, J. Appl. Phys. **111**, 07A948 (2012)
97. R.F. Wallis, in *Surface Magnetoplasmons on Semiconductors*, ed. by A.D. Boardman. Electromagnetic Surface Modes (Wiley, New York, 1982)
98. M. Kushwaha, P. Halevi, Phys. Rev. B **36**, 5960 (1987)